Bulletin of Earthquake Engineering
https://doi.org/10.1007/s10518-026-02397-w

ORIGINAL ARTICLE

Seismic performance of a foundation shoe connection for precast columns combining starter bolts and grouted corrugated ducts

Luca Facconi[1] · **Paolo Pizzini**[1] · **Fausto Minelli**[1]

Received: 23 April 2025 / Accepted: 1 February 2026

Abstract
The use of dry-assembly systems to connect precast concrete columns to foundations has become a common method for constructing commercial and industrial buildings. In such structures, the column base is a critical section, as the design typically follows a cantilever frame arrangement where columns are fixed to the foundation and hinged to beams supporting the floors. Consequently, column-to-foundation connection systems must resist both static and seismic forces, allowing the columns to develop the plasticity and energy dissipation capacity required to meet seismic demands. This study introduces a novel precast column-to-foundation connection system adopting steel bolted shoes and intermediate rebars grouted into the foundation during on-site installation. Unlike existing systems, the proposed design employs only four steel shoes welded to the longitudinal corner rebars of the column. The research involved two reverse cyclic tests on precast columns constructed with the proposed connection system. Two different connection configurations were investigated: the former adopted only the four bolted steel shoes; the latter combined the four bolted shoes with intermediate rebars grouted into corrugated ducts embedded in the foundation. The tests evaluated resistance, energy dissipation capacity, displacement and curvature ductility as well as the failure mechanisms governing the behavior of entire column-foundation assembly subjected to simultaneous combination of axial and bending actions. Additionally, an analytical approach to determine the plastic hinge length suitable for columns provided with the adopted precast connection was proposed. Finally, a beam model with lumped plasticity was developed to simulate the monotonic response of precast columns using the proposed connection system.

Keywords Precast concrete · Columns · Column-to-foundation joint · Seismic · Cyclic test · Lumped plasticity

Extended author information available on the last page of the article

Published online: 18 February 2026

1 Introduction

Industrial and commercial buildings worldwide have been widely constructed with precast Reinforced Concrete (RC) elements. Compared to traditional RC structures, precast systems generally allow reduced construction time and costs while also ensuring enhanced safety due to the quality controls performed during precast production. For precast buildings, the structural system usually consists of cantilever columns (Belleri et al. 2015; Dal Lago, Toniolo and Lamperti Tornaghi 2016) that are fixed at the base and pinned to the roof and floor beams supporting the different stories of the constructions. From a seismic design perspective, columns represent the main elements resisting the horizontal forces induced by the seismic action. When a cantilever is subjected to lateral actions, the maximum demand of deflection capacity and resistance is concentrated at the column base section which, therefore, represents the most critical region of the structure (Toniolo and Colombo 2012). Seismic events in recent decades, such as the 2012 Emilia earthquake (Magliulo et al. 2014; Savoia, Buratti and Vincenzi 2017), have highlighted the crucial role of connections in determining seismic performance and have stressed the importance of adequate detailing in design, particularly for the column-to-foundation connection system. These connections (e.g., monolithic, precast joints, etc.) must be able to develop adequate ductility, energy dissipation capacity and resistance to withstand the seismic demand and ensure the effective transfer of actions from the column base to the concrete foundation (Deng et al. 2022; Nascimbene and Bianco 2021).

Traditionally, precast columns are positioned within RC pocket foundations and rigidly connected using cast-in-place concrete to fill the gap between the column base and foundation. While structurally effective, this method has proven to be less feasible for multi-storey buildings requiring large foundations. Additionally, it presents challenges and criticisms due to the complex and time-intensive operations needed for positioning, erecting and levelling columns on-site. An alternative to traditional techniques is the use of dry or semi-dry assemblies (Dal Lago, Negro and Dal Lago 2018) that incorporate base plates, similar to the bolted connections commonly used in steel-framed structures. These assemblies are part of the structural detailing of the RC column as they usually consist of steel plates and/or sleeves that are connected to the longitudinal reinforcement before concrete casting. From the practical point of view, these precast connection systems simplify construction operations as they offer temporary support to the RC column and allow for easy adjustments to ensure the column's vertical alignment during erection.

The literature reports several studies showing the seismic performance of the precast connections systems. Among the others, the connection systems adopted in common practice include the use of either grouted sleeves/ducts (Belleri and Riva 2012; Fan et al. 2020; Liu et al. 2022; Tullini and Minghini 2020; Kurama et al. 2018; Metelli, Beschi and Riva 2011) or bolted connections consisting of steel plates or shoes cast within the RC column and connected to the foundation by bolts (Dal Lago, Toniolo and Lamperti Tornaghi 2016; Nascimbene and Bianco 2021; Pul et al. 2021).

This paper discusses the results of an experimental investigation focusing on the seismic behavior of two precast RC columns provided with a column-to-foundation connection (see Sect. 2) consisting of four steel shoes and grouted rebars. The two specimens differ in the number of longitudinal bars of the column anchored to the foundation. In the first specimen (i.e., PC1), the column is connected to the foundation exclusively through four bolted

steel shoes located at the corners of the column cross-section. In contrast, the second specimen (i.e., PC2) incorporates both the four corner shoes and additional intermediate bars along the four sides of the column cross-section. Specimen PC1 does not represent a typical connection configuration used in practice; rather, it isolates and highlights the structural performance of the steel shoes only. Conversely, the novel combination of corner shoes and intermediate grouted bars included in the specimen PC2 is representative of connection detailing commonly used by designers in precast systems. The seismic performance of the two specimens was assessed by quasi-static reverse cyclic tests aimed at simulating the behavior of the cantilever column subjected to the combination of a constant axial load and a lateral point load applied at the top end. The results of the experimentation will be described and discussed in detail to highlight the contribution provided by the adopted connection sub-assembly to the overall response of the specimen. Besides the data obtained from the conventional instrumentation, the analysis of results will take advantage of strain measurements detected by the Digital Image Correlation (DIC) method, which allowed the progressive detection of the evolution of the concrete crack pattern particularly in the area of the joint. Considerations on the capacity, displacement and curvature ductility, dissipated energy and the equivalent viscous damping will be reported and discussed.

Eventually, based on the lumped plasticity approach (Cimmino, Magliulo and Manfredi 2020), a beam model suitable for implementation in non-linear finite element analysis (pushover) of RC frames will be developed. An equation to calculate the plastic hinge length will be proposed to predict the rotation of the plastic hinges included in the model. Model validation will be carried out through comparison with the load-deflection envelope curves obtained from the tests.

Considerable research has been conducted on the behavior of foundation connections for precast RC columns. However, when considering precast connections like that presented herein, steel shoes are always used to anchor all the column rebars to starter bolts located in the foundation. This work shows that the complexity of the precast joint can be considerably reduced by combining the traditional steel shoes, which are used to connect only the corner rebars, with grouted corrugated ducts anchoring the intermediate rebars within the column cross-section. The results of the present research demonstrate that the proposed "hybrid" solution is effective in providing the RC column with an adequate seismic performance. Moreover, the analytical model presented in the final section of the paper offers a useful tool for researchers and practitioners to predict the seismic behavior of columns using this connection system.

2 Description of the precast connection and novel features

Figure 1a shows a square precast RC column, typically used in practice, which is provided with longitudinal rebars located both at the corners and at intermediate positions along the sides of the cross section. The figure also highlights the main features of the connection adopted in this research to join the column to a cast-in-place RC foundation. The connection system consists of four steel shoes located at the corners of the base section and welded to the corner rebars of the column. As shown in Fig. 2, the shoe is made of three S355 grade steel plates (i.e., nominal yield strength of 355 MPa according to EN10025-2 (2019)) joined together by fillet welds having a leg length of 10 mm. The base plate of the

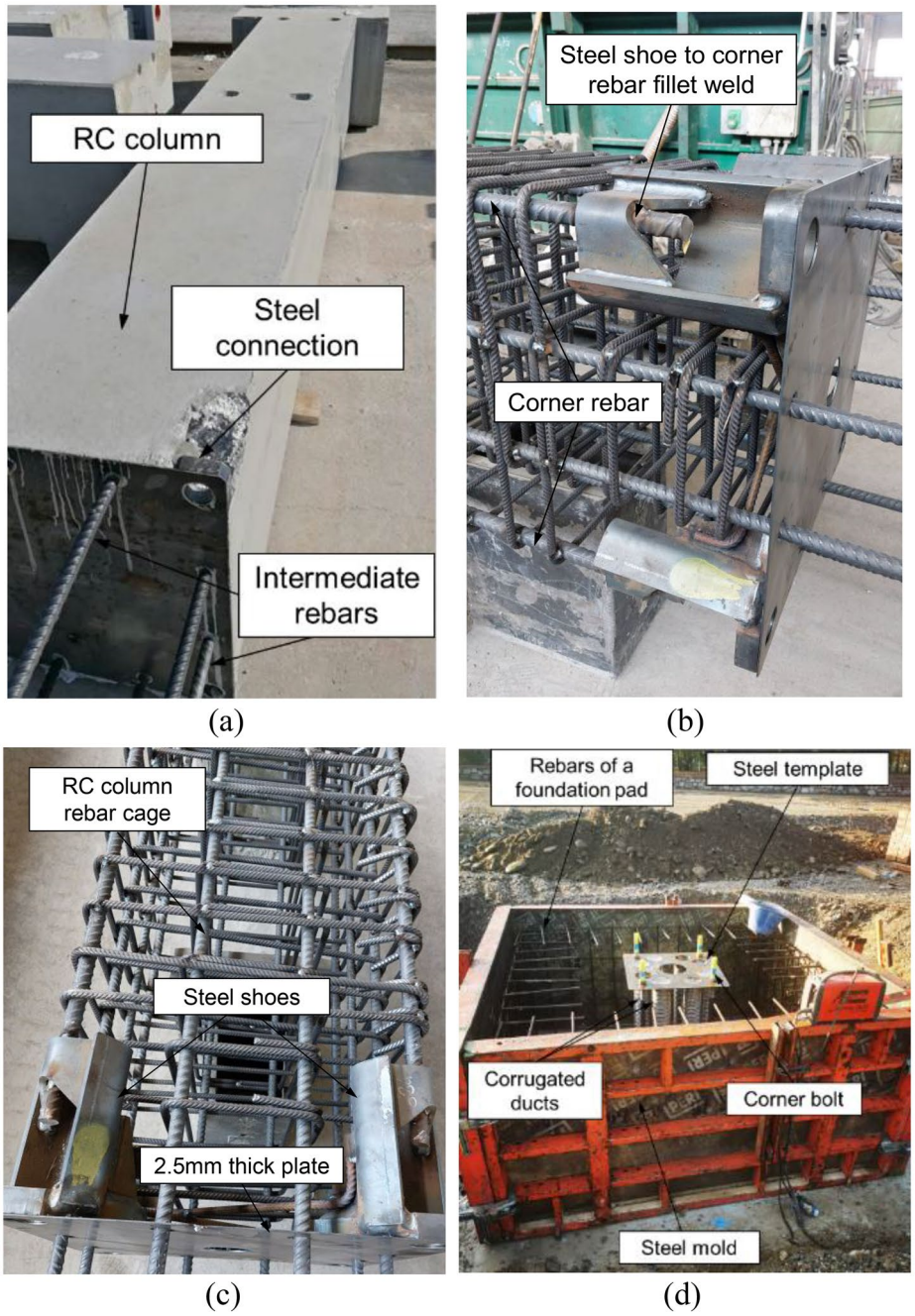

Fig. 1 (**a**) View of a precast column with intermediate rebars. View of the column's rebar cage including the steel connection: (**b**) top view; (**c**) side view. (**d**) Corrugated ducts and hold-down corner bolts positioned in the rebar cage of a RC foundation

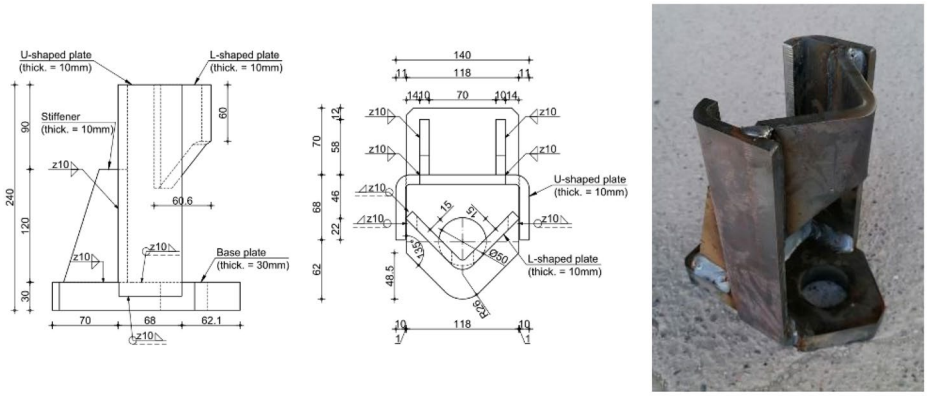

(a) (b) (c)

Fig. 2 Schematic of the steel shoe (dimensions in [mm]): (**a**) side view; (**b**) top view; (**c**) actual view. Welding symbols according to EN ISO 2553:2019

shoe is 30 mm thick and features a 50 mm diameter through-hole for the anchoring bolt cast within the RC foundation. A vertical U-shaped plate, 10 mm thick, is welded to the base plate and is provided with two stiffeners to enhance the bending stiffness and resistance of the U-shaped section. Finally, an L-shaped plate, also 10 mm thick, is welded to the top side of the U-shaped plate, allowing the connection of the corner rebar to the shoe by a couple of fillet welds. These welds ensure the transfer of shear stresses between the rebar and the L-shaped plate. Additionally, a 2.5 mm thick square plate with a side length of 600 mm is welded to the bottom side of the four shoes to keep their correct position during concrete casting. Note that this base plate is usually provided with holes that are crossed by the intermediate rebars of the column. Both the shoes and the bottom plate are welded to the steel reinforcement cage of the column before placing it in the mold (Fig. 1b and c). After casting operations, which are performed in pre-casting factories, the connection system becomes fully integrated with the RC column (Fig. 1a). The connection adopted here differs from other similar bolted socket-based systems (Dal Lago, Toniolo and Lamperti Tornaghi 2016; Nascimbene and Bianco 2021) available on the market by using four steel shoes located only at the corners of the column base section. Intermediate rebars, if any, protrude from the base side of the column to be inserted into the corrugated ducts positioned in the foundation.

The column is generally installed on RC pads or strip foundations constructed on site. The holding-down steel bolts and the corrugated metal ducts are vertically positioned in the foundation cage (Fig. 1d) using a template steel plate, which ensures their correct alignment during the construction process. Once the foundation has been cast, the precast column is lowered through a crane onto the foundation so that the intermediate rebars of the column are gradually inserted in the corrugated ducts. Each bolt is fastened to the steel shoe by a hexagonal nut provided with a flat square washer with a side length of 60 mm, installed on the upper side of the base plate of the shoe (Fig. 3a). A nut and washer are also screwed onto the lower side of the base plate to adjust the column position before locking the upper nut.

After clamping the four shoes, temporary formwork is constructed around the base of the column and a low-shrinkage cement-based mortar is then poured beneath the base plate (Fig. 3b). The thickness of the grouting layer placed under the base plate generally ranges

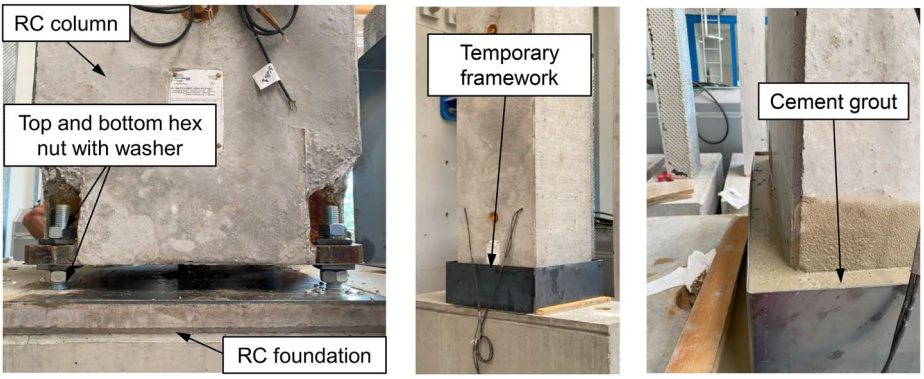

Fig. 3 (**a**) View of the connection after completing clamping and levelling operations. (**b**) Cement grout poured in the temporary mold

from 40 to 50 mm. The height of the temporary mold is selected so that the grout completely covers the four steel shoes. Grouting is essential for sealing the joint, protecting steel rebars from corrosion, and forming a strong, compact base between the base plate and the RC foundation. Therefore, before installing the column, water must be removed from the corrugated ducts to prevent a reduction in grout strength due to an increased water-to-cement ratio. Once the grout has sufficiently hardened, typically a few hours after pouring, the formwork can be removed.

The connection system described above appears to be similar to others presented in the literature and already available in the market. However, the following novel features can be clearly recognized:

- The steel shoes are specifically designed to minimize the eccentricity between the corner rebars of the column and the bar connecting the base plate to the foundation. This is achieved by appropriately adjusting the dimensions of the "L-shaped" components that form the shoes (Figure 2).
- Unlike other systems on the market, which adopt a steel shoe for each bar crossing the column base, the system proposed herein uses four steel shoes to connect only the corner rebars to the foundation. This solution allows minimizing the number of bolted connections required to properly level the column during the positioning phase.

3 Experimental program

To investigate the seismic behavior of the steel connection described above, two specimens were tested in the Laboratory "P. Pisa" of the University of Brescia under reversed cyclic quasi-static loading conditions. The two samples aimed at simulating a typical precast column of a multi-storey building joined to the RC foundation by the proposed connection system. To represent the behavior of a typical cantilever column supporting floor girders, the test set-up was designed to fully restrain the base of the test columns. As described in the following sections, the two specimens differ for the layout of rebars crossing the base plate

of the joint. The first specimen, hereafter referred to as PC1, presents no intermediate bars crossing the joint and anchoring to the foundation. PC1 serves as a reference specimen that allows to highlight the ability of the four shoes to transfer internal actions to the foundation and enable the development of plastic deformations. The second specimen, named as PC2, represents a configuration typical of actual applications, which includes intermediate rebars grouted to the foundation. In this case, the cyclic test is expected to prove the resistance and displacement capacity of the connection when steel shoes are combined with rebars. The effectiveness of this combination is closely related to the actual bond strength developed at the grout-to-rebar interface.

The present section will describe the main geometrical and material properties of the two specimens, including a detailed description of the set-up adopted to perform and monitor the cyclic tests. A separate section of the manuscript (i.e., Sect. 4) will be entirely devoted to the analysis and discussion of the experimental test results.

3.1 Specimen geometry

The schematic of Fig. 4 shows the geometry of the two full-scale specimens (i.e., PC1 and PC2) tested in the present research. Each specimen is composed of a RC footing, which is clamped to the laboratory strong floor, and a RC column having a total height (steel connection included) of about 2090 mm and a square cross-section with a side length (h) of 600 mm. Reinforcement detailing was designed to fulfill the minimum requirements recommended by the Italian structural code NTC2018 (2018) for the critical regions of primary columns with high dissipative capacity (i.e., Ductility Class "CDA" corresponding to the Ductility Class High "DCH" defined by EN 1998-1 (2004). Longitudinal reinforcement consists of 24 mm diameter (Ø24) corner rebars and two 20 mm diameter (Ø20) intermediate rebars along each column side. Stirrups with a diameter of 12 mm (Ø12) and a total of four legs are placed over the height of the column with a spacing of 100 mm. Stirrup spacing is reduced to 50 mm in the concrete region located at the column base, between the steel shoes of the joint. To prevent sliding phenomena occurring at the column base and minimize the effect of shear on the flexural behavior of the connection, an 80 mm diameter steel dowel with a smooth surface is placed at the center of the cross-section. The smooth surface of the dowel reduces its contribution to the flexural resistance of the column.

During column installation, a shear dowel is inserted into a 140 mm diameter corrugated duct, which is placed in the center of the foundation and then joined to it by grouting. The steel shoes of both specimens are bolted to the RC foundation using four M30 threaded rods (30 mm in diameter) made of 8.8 grade steel. These rods are cast-in-place with the RC foundation. To secure the shoes to the M30 rods, two hex nuts are used, each paired with a 60x60x10 mm^3 steel washer. These nuts are tightened on the top and bottom sides of the shoe base plate, respectively. Note that the bottom nut is also used to adjust and level the column during installation.

The specimen PC2 (Fig. 4b) differs from PC1 (Fig. 4a) in that it has intermediate rebars connected to the foundation. As shown in Fig. 4b, the intermediate rebars extend approximately 944 mm from the bottom side of the column. Similar to the shear dowel, these rebars are inserted into vertical corrugated ducts placed in the foundation and are joined to it by grouting.

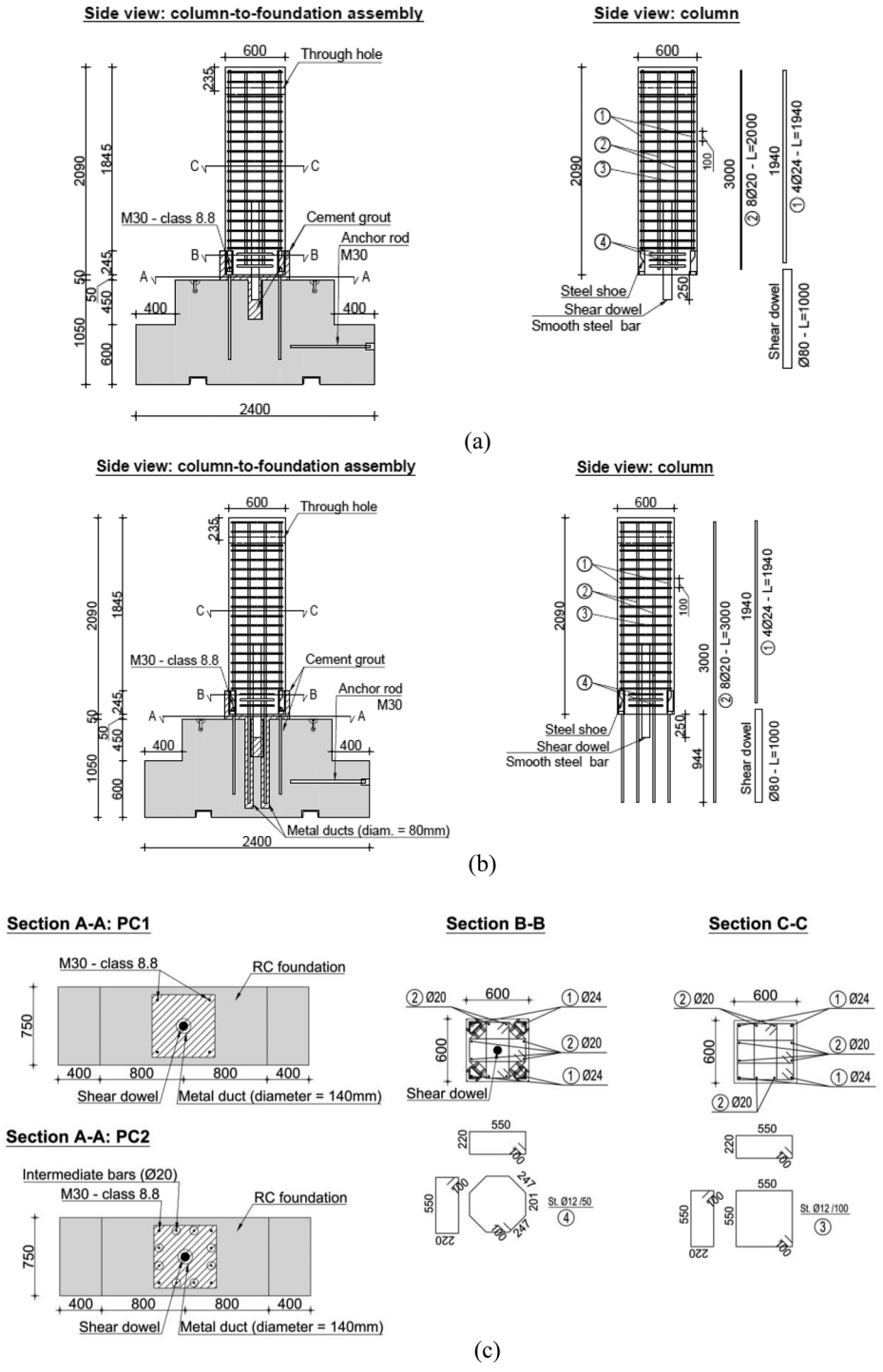

Fig. 4 Geometry and reinforcement details of the specimen (**a**) PC1; (**b**) PC2; (**c**) cross-section of both specimens. (dimensions in [mm])

A through hole crossing the whole width of the cross-section is located in the middle of the column, at 235 mm from the top side (Fig. 4a). This hole is aligned with the electromechanical jack used to apply the horizontal cyclic load (see Sect. 3.3).

3.2 Material properties

The concrete used to construct the specimens was cast and initially cured in the precast factory. A total of four 150 mm cubic specimens were prepared from the same concrete batch used for each test column and were then tested under uniaxial compression. The cubes of the specimen PC1 and PC2 were tested after 33 and 40 days from the casting. Table 1 reports the mean cube strength ($f_{cm,cube}$) obtained from the characterization tests as well as the corresponding cylindrical mean compressive strength (i.e., $f_{cm}=0.83\cdot f_{cm,cube}$). The mean secant Young's modulus (E_{cm}, secant between compressive stress values of zero and $0.4\cdot f_{cm}$) and the tensile strength (f_{ctm}) were both calculated according to the EN 1992–1-1 (EC2, 2023). In more detail, the elastic modulus can be calculated as $E_{cm}=k_E\cdot(f_{cm})^{0.3}$, where k_E is a constant equal to 9500 for quartzite aggregate. The mean uniaxial tensile strength results from the relation $f_{ctm}=0.3\cdot f_{ck}^{2/3}$, where f_{ck} is the characteristic cylindrical compressive strength calculated with the normal distribution reported in EN 1990 (2023) ($f_{ck}=f_{cm}\cdot[1\text{-}kn\cdot CV]$, with kn = 1.83 for four specimens and CV = coefficient of variation) . The CV was calculated as the ratio between the sample standard deviation to the mean value.

A pre-blended thixotropic mortar (Mapefill® Zero) in powder form was used to prepare the grout injected at the base of the column. The pre-mixed mortar contained high-strength cement and expansive additives to mitigate shrinkage cracking. Based on the information reported in the product technical datasheet, mortar has a nominal compressive cube strength (after 28 days curing) of 80 MPa and an elastic modulus of 28 GPa. During the preparation of the grout for test column PC2, eight 100 mm cubes and nine 60x60x140 mm^3 prisms were cast. These specimens were then tested under uniaxial compression and flexure, respectively, after 28 days of curing in a chamber maintained at 20 °C and 90% humidity.

Table 1 Experimental characterization of materials: summary of mean properties

		PC1	PC2
Concrete	$f_{cm,cube}$ (MPa)	78.8 (CV = 4.0%)	71.3 (CV = 7.0%)
	f_{cm} (MPa)	65.4	59.2
	f_{ck} (MPa)	60.6	51.6
	f_{ctm} (MPa)	4.6	4.2
	E_{cm} (MPa)	33,300	32,300
Cement grout	$f_{cm,cube}$ (MPa)	-*	66.6 (CV = 3.0%)
	f_{cm} (MPa)	-*	55.3
	f_{ck} (MPa)	-*	52.4
	f_{ctm} (MPa)	-*	4.2
	E_{cm} (MPa)	-*	31,660
	f_{flm} (MPa)	-*	7.7 (CV = 17.7%)
Rebars (Ø20)	f_y (MPa)	-	524.8 (CV = 0.2%)
	f_u (MPa)	-	624.8 (CV = 0.2%)
	ε_u (%)	-	11.8 (CV = 5.0%)
Rebars (Ø24)	f_y (MPa)	526.7 (CV = 0.3%)	511.2 (CV = 0.1%)
	f_u (MPa)	633.7 (CV = 0.2%)	625.4 (CV = 0.1%)
	ε_u (%)	12.3 (CV = 3.0%)	15.7 (CV = 6.0%)

*Data not available

The mean compressive cube strength was used to determine the elastic modulus and the uniaxial tensile strength by means of the same EC2's relationships for concrete reported above. When determining the characteristic compressive strength (f_{ck}), the coefficient kn was assumed equal to 1.74 (i.e., value for eight samples) according EN 1990 (2023). The tensile strength f_{ctm} was calculated by the relation reported above whereas the modulus of rupture (f_{flm}) was determined by testing the nine prisms under three-point bending according EN 196-1 (2016).

As recommended by the NTC2018 (2018), steel rebars with grade B450C (i.e., characteristic nominal yield strength = 450 MPa; ductility class "C" according EC2) were adopted for the two columns. Uniaxial tensile tests UNI EN ISO 15630-1 (2019) were carried out to determine the mean yield strength (f_y), the mean tensile strength at rupture (f_u) and the mean value of the minimum elongation at maximum resistance (ε_u). Table 1 reports the mechanical properties obtained by testing a total of three Ø24 rebar samples taken from column PC1 and four Ø24 and Ø20 samples collected from the column PC2. Based on these data, the expected mean yield strain for rebars is about 2.5 10^{-3}.

The threaded bars M30 (diameter = 30 mm) and the hex nuts are made of high strength medium carbon steel with grade 8.8. According to EN ISO 898-1 (2013), this grade corresponds to a minimum characteristic yield and rupture tensile strength of 640 MPa and 800 MPa, respectively.

Finally, the steel shoes and the column's base plate were fabricated from structural steel grade S355, which has characteristic nominal yield and ultimate strengths of 355 MPa and 510 MPa, respectively.

3.3 Test set-up and instrumentation

An overview of the test set-up adopted to perform the cyclic tests is shown in the schematic of Fig. 5. The specimens were positioned in front of the 8 m high RC reaction wall located inside the laboratory and fixed to the strong floor by four Dywidag bars (i.e., two bars per each side of the foundation) clamped to a couple of horizontal steel beams laid on the RC foundation of the column. A pre-tension load of 100 kN was applied to each Dywidag bar. To prevent horizontal sliding of the foundation, two horizontal steel bars were installed to connect the foundation to the reaction wall. Conversely, to counteract sliding in the negative loading direction, a reaction RC beam was placed on the floor between the foundation and the reaction wall. A 500 kN capacity electromechanical screw jack fixed to the reaction wall was used to apply the horizontal load to the top-end of the column. As shown in Fig. 5, the horizontal load was applied at a height (L) of 1905 mm from the top surface of the foundation, resulting in a shear span to depth (h = 600 mm) ratio (L/h) of 3.2. A double-hinged steel tubular element provided with a load cell connected the screw jack to the top of the column. Two hollow cylindrical hydraulic jacks placed vertically on a steel spreader beam applied a total axial load (N) of 300 kN, which was kept constant during the test and continuously monitored by a load cell installed at the top of each jack. The two vertical jacks were anchored to the strong floor through Dywidag bars screwed into a steel hinge located at their base (see Fig. 5).

The schematic of Figure 5 shows the position of the instrumentation used to monitor the specimens. As mentioned above, the horizontal load was continuously detected by a load cell installed between the electromechanical jack and the double-hinged connection. The

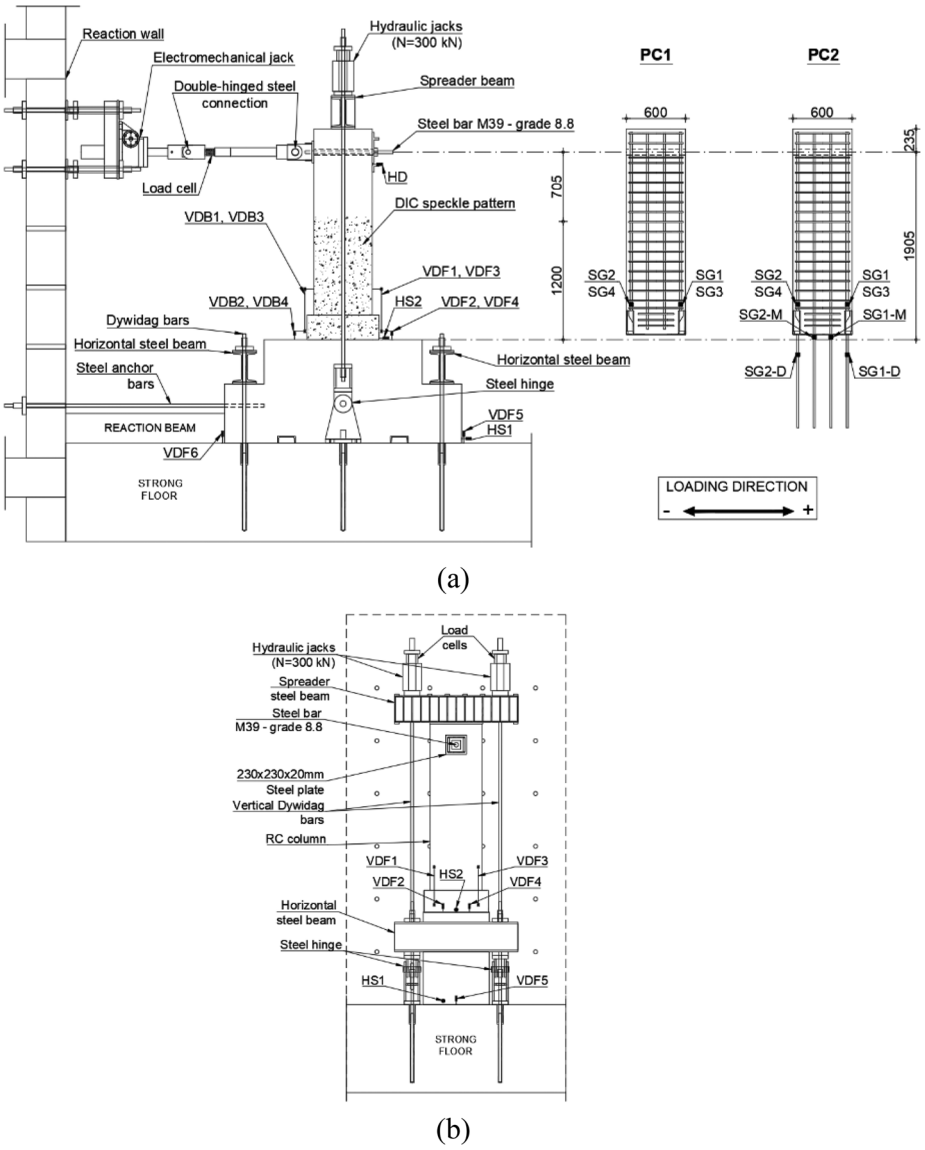

Fig. 5 Test set-up: (**a**) right-side view; (**b**) front view. (dimensions in [mm])

screw jack enabled the test to be conducted under deflection control, allowing the column to be laterally displaced at a rate of 0.05–0.1 mm/s. The lateral deflection (δ) was measured using a horizontal LVDT, referred to as HD, which was installed at a height of 1780 mm from the top face of the foundation. The loading histories of the two specimens, defined by the lateral Drift ratio (D=δ/1780 mm) against the number of loading cycles, are shown in Fig. 6. As one may note, the loading protocol consisted of repeated reverse cycles of stepwise increasing drifts, ranging from a minimum of 0.01% to a maximum of about 3.5–3.7%

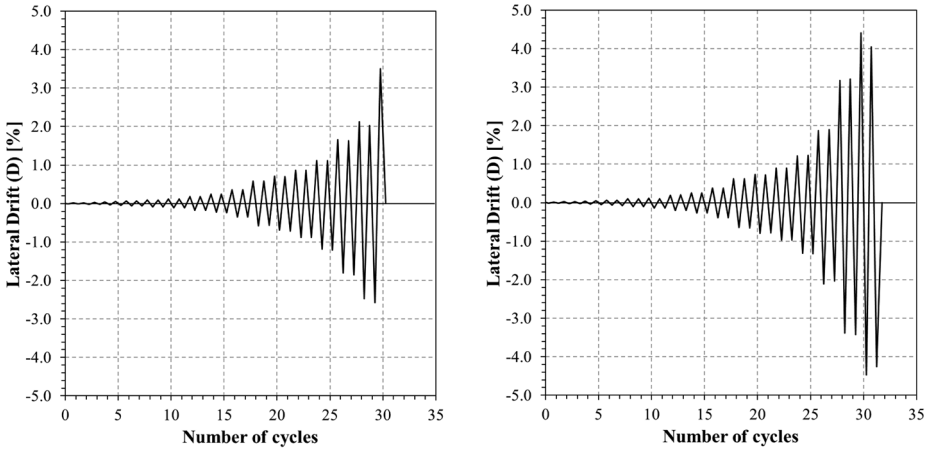

Fig. 6 Loading histories: (**a**) specimen PC1; (**b**) specimen PC2

attained after severe damaging of the column base connection. As recommended by FEMA 461 (2007) for quasi-static cyclic testing, two cycles at each drift amplitude were performed and the number of drift increments in the two loading histories was larger than 10 (i.e., 17 increments for both specimens).

To measure the vertical deflection at the base of the column, a total of eight linear potentiometers were installed on the front (i.e., instruments VDF1 to VDF4) and back (i.e., instruments VDB1 to VDB4) side of the column. The instruments VDF1, VDF3, VDB1 and VDB3 span a length of 500 mm that allows measuring the vertical deformations exhibited by the whole connection system and of the column portion located right above it. The potentiometers VDF2, VDF4, VDB2 and VDB4 present a gauge length of 80 mm, which was selected to measure the deformations occurring over the base plate of the steel joint. The potential relative sliding of the column over the top surface of the foundation was detected by the linear potentiometer HS2. The linear potentiometer HS1 detected horizontal sliding occurring between the floor and the foundation. The uplift of the foundation from the floor was detected by the potentiometers VDF5 and VDF6. Finally, a series of strain gauges were welded to some rebars forming the reinforcing cage of the column to continuously detect the axial strain of reinforcement in the most critical regions of the specimen. About specimen PC1, a total of four strain gauges (i.e., SG1, SG2, SG3, SG4) were installed on each corner rebar of the column to measure the strains acting right above the steel shoe. Additional four strain gauges were installed on the specimen PC2 to monitor the deformation occurring in the intermediate rebars at the column-to-foundation interface (i.e., SG1-M and SG2-M) and in two sections of intermediate rebars located within the grouted ducts (i.e., SG1-D and SG2-D).

To get refined data about the evolution of the strains occurring in the area of the precast connection, a Digital Image Correlation (DIC) system was adopted. A high resolution 50 Megapixels CMOS (Complementary Metal–Oxide–Semiconductor) sensor camera was used to take pictures of the panel surface at 15–30 s intervals. The camera was mounted on a tripod placed at 2 m from the monitored surface and oriented with its optical axis normal to

the right-side of the column. To have sufficient contrast between the lightest (white) and the darkest (black) regions of the DIC pattern, two white led lights were placed on the right and left side of the camera so that they provided a uniform and constant lighting of the specimen surface. The speckle pattern was prepared by spraying black paint on part of the right-side surface of the column (see Fig. 5a) that was previously painted white.

4 Test results and discussion

4.1 Load-deflection response and damage evolution

Figure 7a shows the hysteretic response (i.e., total base shear (V) vs. lateral deflection (δ)) of the specimen PC1. Key points labeled A, B, C, and D are marked on the curve to highlight the most significant events observed during the test. The initial response appears linear and symmetric in both loading directions except for a slight loss of stiffness occurring at point A' (V = +40 kN; δ = +0.4 mm; D = +0.02%) that is related to the formation of a flexural crack at the column base, as detected by the potentiometers VDB2 and VDB4. This mechanism is likely activated due to initial settlement (e.g., bolt sliding, bolt relaxation) of the corner bolts on the back side of the column. The points A^+ (V = +110 kN; δ = +2.0 mm; D = +0.11%) and A^- (V = −108 kN; δ = −1.5 mm; D = −0.08%) are associated with the onset of the first flexural cracks developed above the steel shoes and clearly emphasized by the DIC contours of Fig. 7b, which highlight these crack locations using warm colors to indicate high tensile strains. The two pictures referred to the points A^+ and A^- show that one primary crack extends over ¼ of the cross section located right above the steel shoes, while a second crack runs parallel to the main one at about 400 mm from the base of the column. As the column is displaced further, a gradual reduction in lateral stiffness is observed due to the development of new flexural cracks over the column height. The DIC contours (Fig. 7b) corresponding to the points B^+ (V = +180 kN; δ = +10.0 mm; D = +0.56%) and B^- (V = −216 kN; δ = −10.0 mm; D = −0.56%) depict these new cracks, along with two vertical cracks that cross the cement grout covering the lateral surface of the connection. It is worth noting that the early loss of stiffness exhibited by the column during the initial positive loading stages caused the base shear at point B^- to be lower than that observed at point B^+. According to the strain gauge measurements, once a lateral deflection of δ = +20.0 mm (V = +200 kN) was attained, the corner rebars located on the back side started to yield, thus attaining an average strain of 2.5×10^{-3}. A similar behavior was observed for the rebars on the front side when a lateral deflection of δ = −21 mm was attained. The maximum resistance was reached at points C^+ (V = +210 kN; δ = +27.0 mm; D = +1.51%) and C^- (V = −226 kN; δ = −21.1 mm; D = −1.17%). The decrease in stiffness and resistance governing the post-peak response is mainly due to the progressive increase in width of the cracks located at the base of the column as well as by crushing of concrete in the compressed part of the column base section. Compared to the post-peak response detected in the positive direction, the resistance decay observed during the negative loading stage appears more pronounced. A possible explanation of this behavior could be the damage of the welds joining the corner rebars to the steel shoes positioned on the front side. Moreover, the column experienced a transversal deflection (i.e., in the left-side direction) that became progressively more pronounced as the lateral deflection increased. This bi-axial bending response of the column contributed to the asymmetry in the

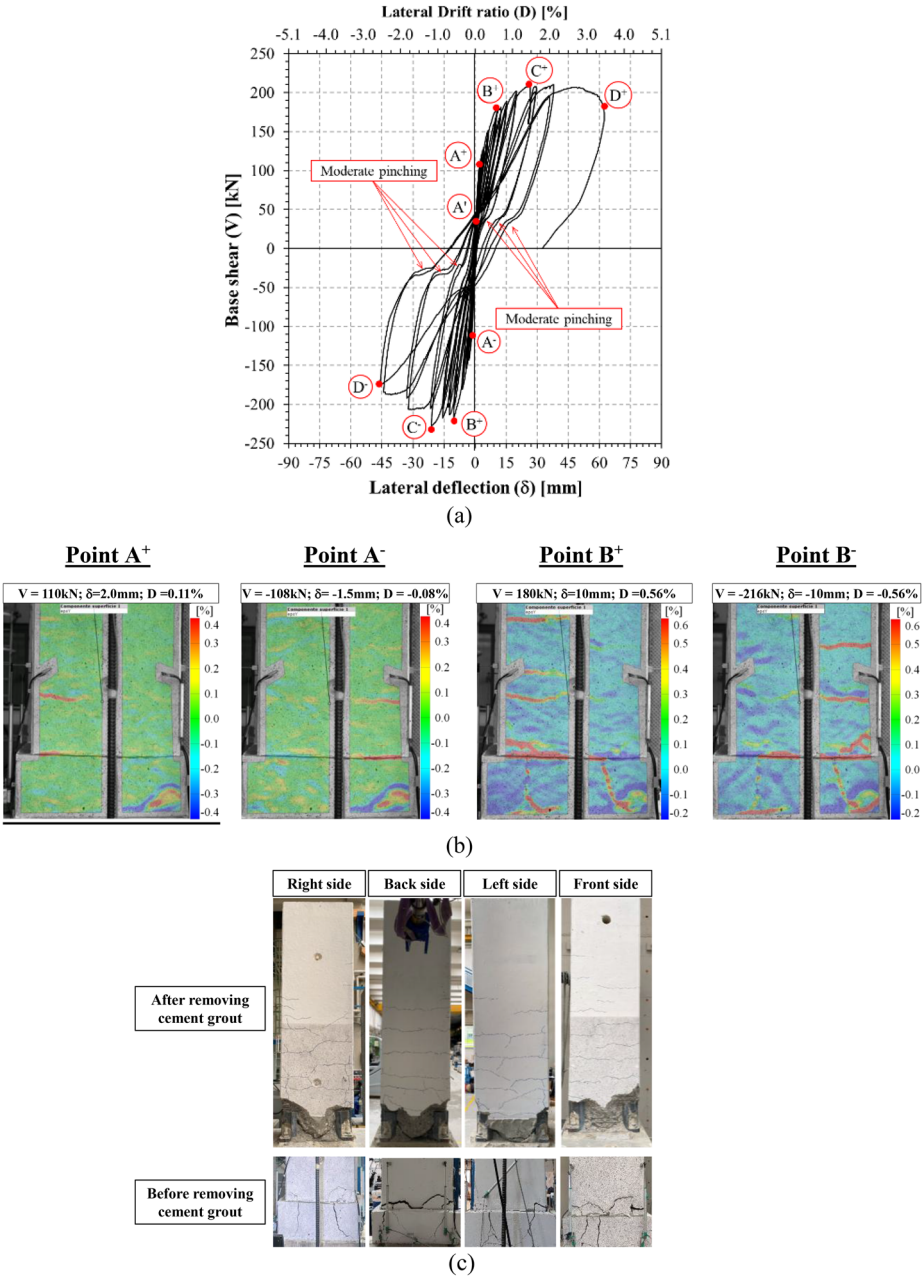

Fig. 7 Specimen PC1 response: (**a**) hysteretic curve; (**b**) contour of vertical strains (scale in [%]) detected by DIC; (**c**) final crack pattern

load-deflection response. It is also worth remarking that the post-peak cycles of the hysteretic response present minor pinching phenomena, which tend to increase as the specimen approaches the ultimate deflection. Pinching in hysteretic cycles is generally attributed to different factors, like shear sliding along cracked sections, delayed closure of two cracked surfaces, partial debonding of rebars, concrete crushing, etc. In addition, as pointed out by other authors (Nascimbene and Bianco 2021), this behavior could be related to the contact loss occurring between the nut/washer on the threaded bars and the base plate of the shoe.

The test ended after attaining points D^+ (V = +171 kN; δ = +62.4 mm; D = +3.51%) and D^- (V = −175 kN; δ = −45.7 mm; D = −2.56%), which correspond to the ultimate deflection of the column. The ultimate crack pattern detected on the four sides of the column is shown in Fig. 7c. This picture puts in evidence the base of the column before and after removing the grout layer surrounding the surface of the specimen. It appears that the horizontal crack located just above the shoes crossed the entire width of the cross section. Moreover, the vertical cracks, which were detected during the test on the outer surface of the cement grout layer, extended through the entire height of the connection, reaching the base of the column. Besides the weld damage mentioned earlier, all four steel shoes also evidenced signs of permanent deformation, particularly around the base plate, which was clearly visible to the naked eye at the end of the test.

The hysteretic response of the specimen PC2 is depicted in Fig. 8a. The key points A^+ (V = +123 kN; δ = +1.9 mm; D = +0.11%) and A^- (V = −107 kN; δ = −1.2 mm; D = −0.07%) correspond to first cracking of the cross section located right above the steel shoes (Fig. 8b). These first cracks and the related loads are very similar to those observed for the specimen PC1. Once again, the reduction of the lateral stiffness occurring after first cracking appears to be more pronounced in the positive loading direction compared to the negative direction. The DIC contours (Fig. 8b) detected at points B^+ (V = +288 kN; δ = +16.0 mm; D = +0.90%) and B^- (V = −378 kN; δ = −17.4 mm; D = −0.98%) show that the increase in lateral deflection occurred after point A led to an evident growth of the flexural cracks above the joint whereas no significant cracks were observed on the surface of the cement grout. The rebars located on the back side of the column started to yield at the first cracked section over the steel shoes once the point B^+ was reached. On the contrary, yielding of rebars located on the opposite side began at V = −330 kN (δ = −13 mm), before attaining point B^-. The attainment of yielding was proved by the data provided by the strain gauges installed on rebars Ø20 and Ø24, which attained axial strains of 0.24–0.25%. Vertical cracks appeared and started to propagate through concrete near the steel shoes after reaching point B. Both events are highlighted by the change in slope of the hysteretic curve. The points C^+ (V = +381 kN; δ = +33.0 mm; D = +1.85%) and C^- (V = −400 kN; δ = −25.0 mm; D = −1.40%) mark the yielding of corner and intermediate rebars intersecting the grouting layer under the base of the joint. The maximum load attained in the positive direction at point D^+ (V = +413 kN; δ = +56.4 mm; D = +3.17%) was followed by a gradual decrease in strength leading to the ultimate load at point E^+ (V = +400 kN; δ = +78.5 mm; D = +4.41%). The maximum negative load was first reached at point D^- (V = −433 kN; δ = −37.3 mm; D = −2.10%) and remained approximately constant up to point E^-, which corresponds to a lateral load V = −436 kN and a deflection δ = −60.0 mm (D = −3.37%). For safety reasons, the test was stopped after attaining point F^- (V = −418 kN; δ = −79.5 mm; D = −4.47%) due to significant transverse deflection resulting from damages at the joint location (see Fig. 8c).

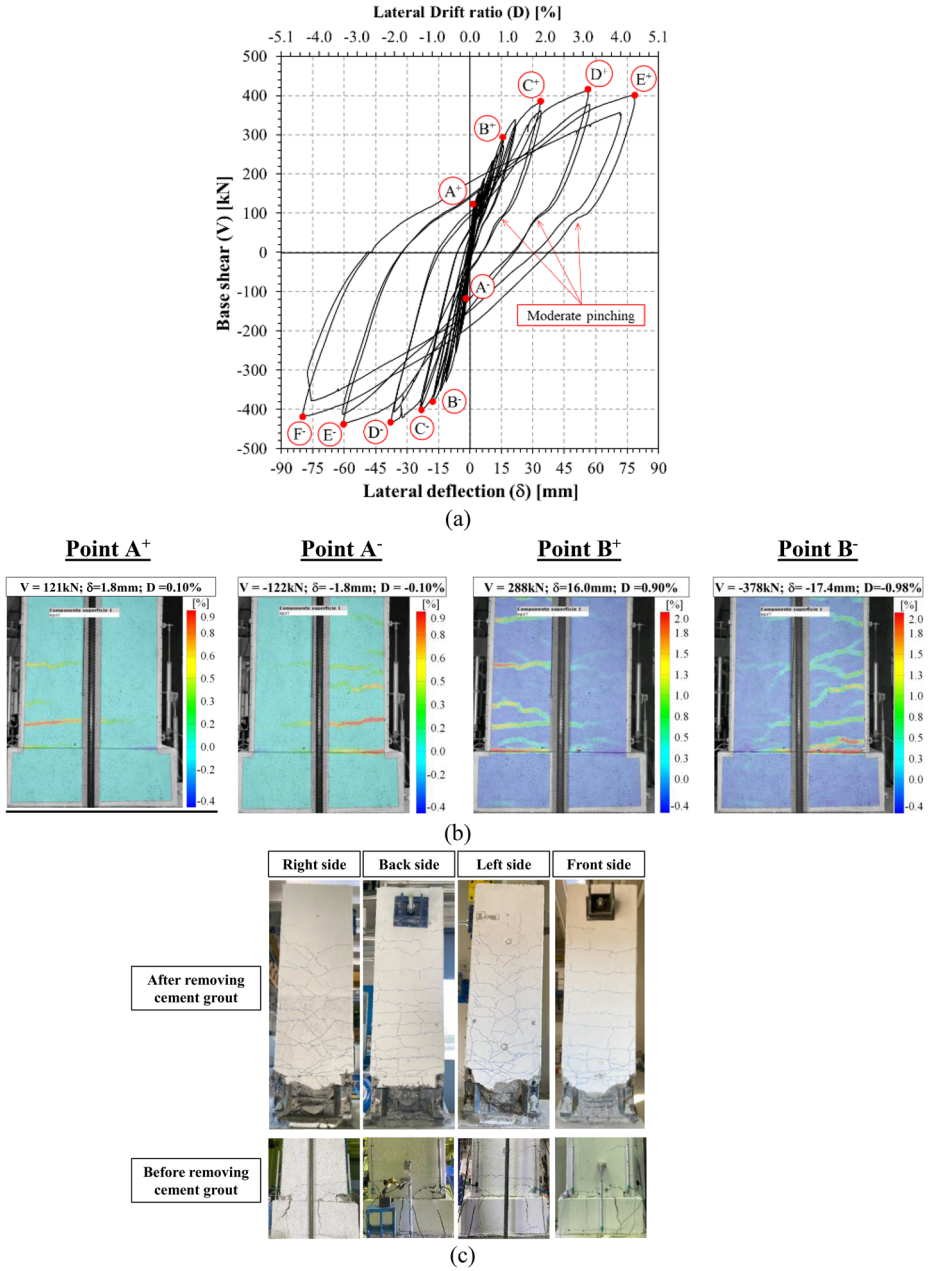

Fig. 8 Specimen PC2 response: (**a**) hysteretic curve; (**b**) contour of vertical strains detected by DIC; (**c**) final crack pattern

The pictures in Figure 8c show the damage pattern observed after the test completion. Except for the higher number of flexural cracks in the concrete, which are likely due to the higher longitudinal reinforcement ratio of the column, the damage at the base of the column appeared to be similar to that seen in specimen PC1. On the opposite, the deformation of the steel shoes due to bending action was significantly more pronounced compared to that observed in PC1. However, in the present case, no cracks or ruptures in the welding between rebars and shoes were observed. Finally, a slight pinching behavior affected only some of the positive loading cycles (Fig. 8a).

The curves enveloping the hysteretic response of the two specimens are represented in Figure 9a along with the corresponding bi-linear curves defined according to the Italian structural code's Commentary (COMM2019, 2019). The bi-linear curve (Fig. 9b) consists of an initial linear branch that extends from the origin to the "yield strength" (V_y), passing through the point (V_{cr}) that corresponds to 60% of the maximum base shear (V_{max}) detected on the actual response (i.e., the experimental envelope) of the structure. The horizontal branch ranges from the deflection at the elastic limit, i.e. δ_y, to the deflection at the Near Collapse Limit State (δ_{NC}), which is the displacement corresponding to a post-peak load not lower than 85% of the maximum load (V_{max}). The deflection (δ_{LS}) defining the Life Safety Limit State is calculated as $0.75\delta_{NC}$. To calculate V_y, the area subtended by the actual curve is set equal to the area beneath the equivalent bi-linear curve. Table 2 reports all these parameters including also the initial stiffness (K_t), which corresponds to the initial slope (i.e., the tangent to the origin) of the experimental envelope, the slope ($K^* = V_y/\delta_y$) defining the elastic branch of the bi-linear curve, the drift D_{NC} corresponding to δ_{NC} and the displacement ductility index (μ_δ) calculated as the δ_{NC} to δ_y ratio. Note that the envelope curves for the positive and the negative loading directions have been analyzed separately.

The results reported in Table 2 show that both specimens presented different K_t values, depending on the loading direction. The negative stiffness resulted higher (i.e., 12% for PC1; 57% for PC2) than the positive stiffness, as previously discussed in this paper. This

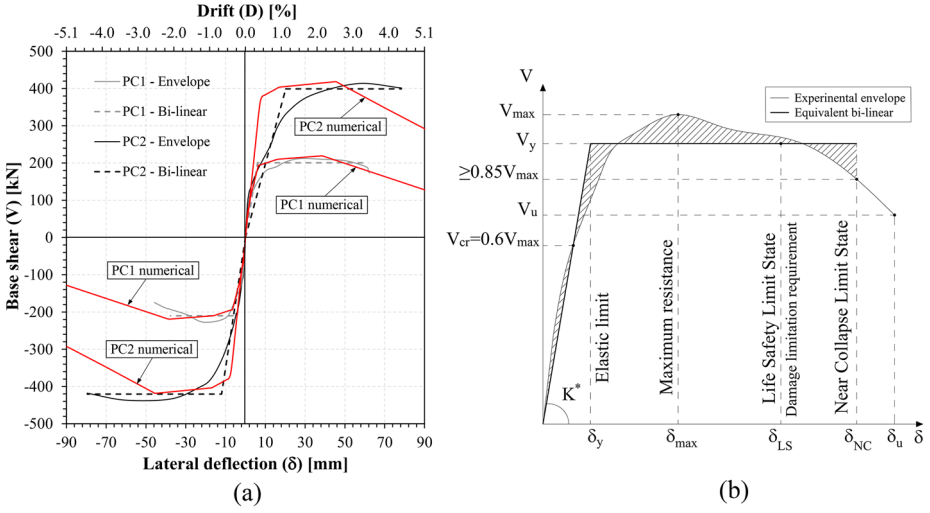

Fig. 9 (**a**) Cyclic curves envelops and corresponding equivalent bi-linear curves. (**b**) Equivalent bi-linear curve according to NTC2018

Table 2 Main results obtained from the tests

Specimen	Experimental envelope					Equivalent bi-linear curve									
	K_t	V_{max}	δ_{max}	V_u	δ_u	K^*	V_{cr}	δ_{cr}	V_y	δ_y	δ_{NC}	D_{NC}	μ_δ	L_P	μ_χ
	$\left[\frac{kN}{mm}\right]$	[kN]	[mm]	[kN]	[mm]	$\left[\frac{kN}{mm}\right]$	[kN]	[mm]	[kN]	[mm]	[mm]	[%]	[-]	[mm]	[-]
PC1 (+)	132	212	26.7	171	62.4	33.4	127	3.8	201	6.1	61.7	3.5	10.1	398	13.2
PC1 (-)	149	227	21.1	175	45.7	50.4	136	2.7	210	4.1	37.6	2.1	9.2	398	12.1
PC1 (Mean)	**140**	**219**	**23.9**	**173**	**54.1**	**41.9**	**131**	**3.3**	**205**	**5.1**	**49.7**	**2.8**	**9.7**	**398**	**12.7**
PC2 (+)	112	413	56.4	402	78.4	19.7	248	12.6	399	20.2	78.4	4.4	3.9	462	4.4
PC2 (-)	176	437	60.2	418	79.5	34.9	262	7.5	420	12.0	79.5	4.5	6.6	462	7.5
PC2 (Mean)	**144**	**425**	**58.3**	**410**	**79.0**	**27.3**	**255**	**10.1**	**409**	**16.1**	**79.0**	**4.4**	**5.3**	**462**	**6.0**

phenomenon could be explained by initial settlement occurring between the steel shoes of the base plate and the nut of the threaded bars. However, by averaging the stiffness values of both loading directions, the stiffness of PC1 (i.e., 140 kN/mm) turned out to be very similar to that of PC2 (i.e., 144 kN/mm). These values are close to those predicted by the elastic theory applied to RC sections. In fact, the second moment of area (J_I) of the uncracked cross-section of the column results to be 11380×10^6 mm^4 and 12148×10^6 mm^4 for PC1 and PC2, respectively. The ratio between the force applied at the top of the column and the corresponding lateral deflection is equal to $3E_{cm} \cdot J_I / L^3$ (L = 1905 mm). Considering this formulation, the elastic stiffnesses of PC1 and PC2 are equal to 162 kN/mm and 169 kN/mm, respectively. The latter are 15–17% higher than the average stiffnesses observed in the tests which, however, are potentially affected by some effects (e.g., settlement of the base plate, concrete pre-cracks) not included in the elastic calculation.

Specimen PC2 presented a mean maximum resistance (425 kN) that was 94% higher than that (219 kN) of PC1. As shown in Sect. 5, this increment of resistance and the values of the maximum resistances are consistent with those predicted by the analytical calculation.

The bi-linearization of the envelope curves highlighted the higher displacement capacity of PC2, which attained a deflection δ_{NC} 59% higher than that of PC1. However, the mean displacement ductility index of the specimen PC2 was 45% lower than that of PC1. This reduction in ductility can be attributed to several factors. First, PC2 had a higher tensile reinforcement ratio (ρ_s=0.54%) compared to PC1 (ρ_s = 0.19%). An increased tension reinforcement ratio generally leads to a reduction in curvature ductility (Park and Paulay 1975), especially in regions where plastic hinges form during loading. Additionally, PC2 exhibited more severe concrete crushing than PC1, as highlighted by the denser crack pattern (see yellow line in Fig. 10) at the base section between the steel shoes. This damage has likely reduced the specimen's ability to develop rotations at plastic hinges, thereby limiting its lateral deflection capacity. Furthermore, PC2 experienced an early loss of initial stiffness during positive loading, which further contributed to the lower ductility index. In addition, one may also consider that the ductility index of specimen PC2 (see Table 2) was probably underestimated as the test was stopped after attaining a 5% reduction of the post-peak capacity instead of 15% required by NTC2018 (2018) for ultimate conditions.

The experimental tests showed that the evolution of damage led to the development of plastic zones that can be lumped in two hinges (Fig. 11) located at the column-foundation interface (i.e., hinge "BS") and close to the top-end of the steel shoes (i.e., hinge "JS"). The hinge "BS" usually activates first. However, hinge relocation may occur if the following relation is fulfilled:

$$\frac{M_{R,JS}}{M_{R,BS}} < \frac{L_{JS}}{L} \tag{1}$$

where $M_{R,JS}$ and $M_{R,BS}$ are the resisting moments of the potential hinges "JS" and "BS", respectively; L_{JS} = 1610 mm is the distance from the center of the plastic hinge "JS" to the point of contraflexure; L = 1905 mm is the total height of the column.

Based on the equation reported in Paulay and Priestley (1992), the curvature ductility (μ_χ) can be related to the displacement ductility by the following relation:

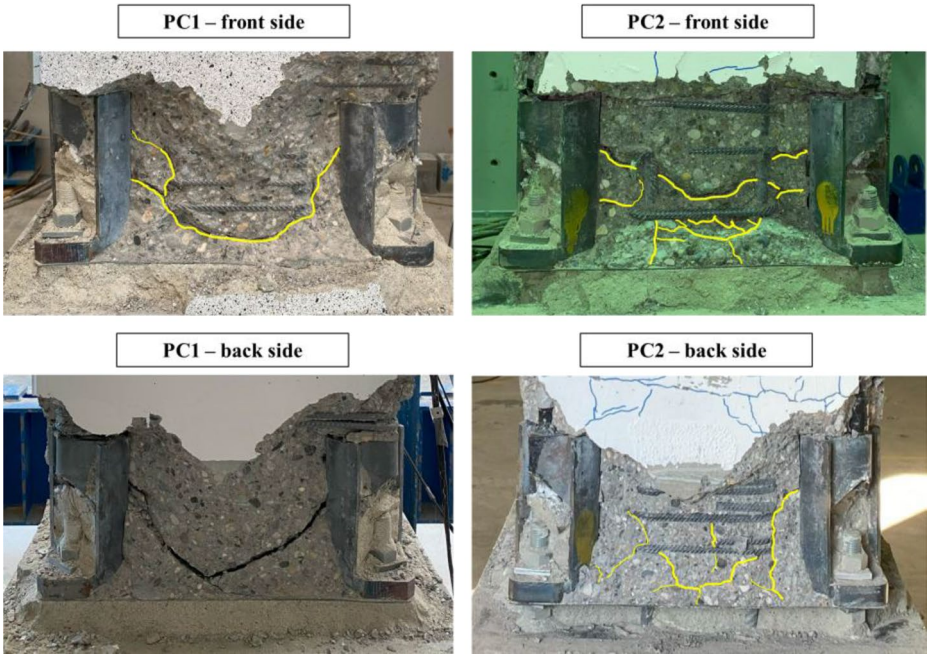

Fig. 10 Damages observed at the base of the specimens following test completion (cracks highlighted in yellow)

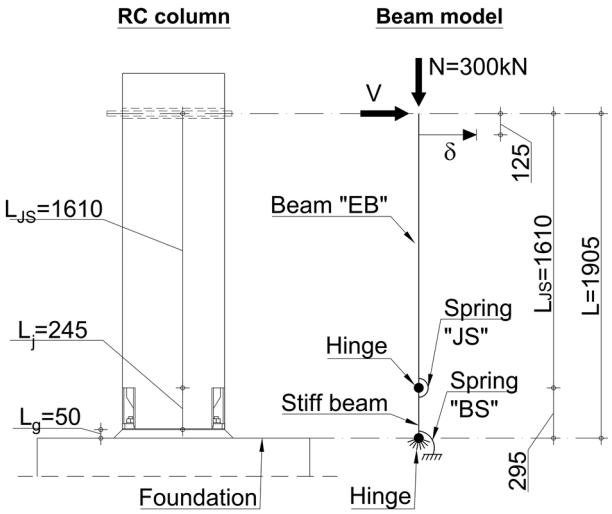

Fig. 11 Schematic of the proposed lumped plasticity model. (dimensions in [mm])

$$\mu_\chi = 1 + \frac{L_{JS}}{3L_P} \cdot (\mu_\delta - 1) \tag{2}$$

where L_P is the effective plastic length, which is here estimated by the following equation adapted from Paulay and Priestley (1992):

$$L_P = \begin{cases} L_{PT} + L_{SP} = L_{PT} + 0.022 \emptyset_l f_y & \text{if } \dfrac{M_{R,JS}}{M_{R,BS}} < \dfrac{L_{JS}}{L} \\ L_g + 0.022 \emptyset_l f_y & \text{if } \dfrac{M_{R,JS}}{M_{R,BS}} \geq \dfrac{L_{JS}}{L} \end{cases} \tag{3}$$

where L_{PT} is the length of the plastic hinge located above the base plate of the joint and L_{SP} is the strain penetration length depending on the diameter ($Ø_l$) and the yield strength (f_y) of longitudinal reinforcement; $L_g = 50$ mm is the thickness of the grout layer laid between the base plate and the foundation. Assuming $Ø_l$ and f_y respectively equal to the nominal diameter (24 mm) and the average yield strength (520 MPa) of bars Ø24, a L_{SP} of 275 mm was obtained for both specimens.

Based on the failure mechanisms observed in the tests, the following relationships are proposed to estimate L_{PT}:

$$L_{PT} = \begin{cases} L_j/2 = 123\text{mm} = 0.22\text{d} & \text{intermediatebars notbonded tothe foundation (i.e., PC1)} \\ L_j/2 + kL_{JS} = 187\text{mm} = 0.34\text{d} & \text{intermediate barsbonded tothe foundation (i.e., PC2)} \end{cases} \tag{4}$$

where $k = 0.2(f_u/f_y\text{-}1) = 0.04 \leq 0.08$ is a reduction coefficient (Priestley et al. 2007) here calculated by considering the mechanical properties of rebars Ø24; $d = 559$ mm is the effective depth of the column cross-section.

The obtained values of L_P and of the curvature ductility are summarized in Table 2. It is worth noting that the ratio between L_P and d was equal to 0.71 and 0.83 for the specimen PC1 and PC2, respectively. Moreover, as expected, μ_δ resulted higher (i.e., 13–30%) than the corresponding μ_χ.

4.2 Dissipated energy and equivalent viscous damping

Reinforced concrete structures are designed to resist earthquake-induced forces by dissipating energy through plastic mechanisms involving concrete damage. This dissipated energy corresponds to the area enclosed within each cycle of the hysteretic response. Figure 12 shows the evolution of dissipated energy versus lateral deflection. For each drift level, the diagrams display the energy (E_{hyst}) dissipated during each loading repetition, namely Cyclic #1 and Cyclic #2. The dotted black line represents the cumulative energy dissipated up to the end of the test. As expected, energy dissipation increases with the lateral drift (D_m) corresponding to the maximum deflection (δ_m) attained by each loading cycle. Notably, energy dissipation becomes significant for drifts above 0.6%. The total cumulative energy dissipated by specimens PC1 and PC2 was 33.5 kJ and 173.7 kJ, respectively. The hysteretic energy can also be expressed using the Equivalent Viscous Damping (EVD) coefficient (ξ_{hyst}), calculated using the area-based formulation adopted by different authors (Jacobsen 1960; Chopra 2011):

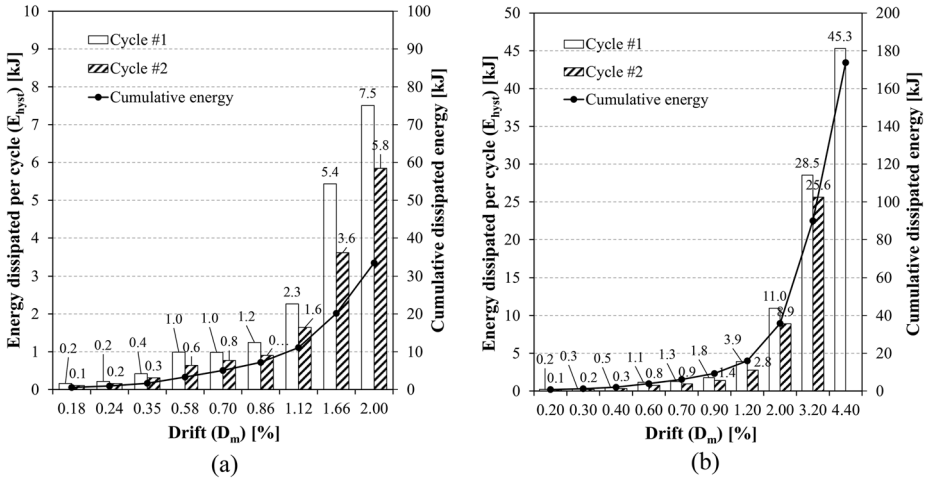

Fig. 12 Evolution of the energy dissipated per each loading cycle and of the corresponding cumulative dissipated energy: (**a**) specimen PC1; (**b**) specimen PC2

$$\xi_{\mathrm{hyst}} = \frac{\mathrm{E_{hyst}}}{2\pi \cdot \mathrm{F}^{+}_{\mathrm{m}} \cdot \delta^{+}_{\mathrm{m}}} \tag{5}$$

Here, E_{hyst} is the energy dissipated in a single cycle, and $F^{+}_{m} \cdot \delta^{+}_{m}$ equals twice the elastic strain energy at the maximum positive deflection of each cycle. This formula equates actual energy dissipation to that of viscous damping under steady-state motion. However, since real earthquakes produce unsteady-state excitations, Eq. (5) may not yield accurate damping values. To improve accuracy, the results from Eq. (5) are multiplied by a correction factor derived from Priestley et al. (2007) and here adapted for the mean ductility values of PC1 ($\mu = 9.7$) and PC2 ($\mu = 5.3$). The corrected EVD values are plotted against lateral drift in Fig. 13.

Figure 13 shows that the corrected EVD of both specimens remained below 10% for drift levels under 0.9–1.2%. Beyond these limits, EVD increased, reaching 16.9% for PC1 and 24.5% for PC2, consistent with findings from similar studies (Nascimbene and Bianco 2021; Belleri and Riva 2012; Fan et al. 2020) on precast connections. At any given drift level, the second loading cycle (Cycle #2) always resulted in lower damping and energy dissipation than the first (Cycle #1), as illustrated in Figs. 12 and 13 (see the bar plots filled with the diagonal line pattern).

5 Numerical modelling

To represent the load-deflection response of the columns, a simple nonlinear beam model based on lumped plasticity can be adopted. The adopted approach assumes that the column does not exhibit shear failure, and the global response of the element is mainly affected by flexural mechanisms occurring within the precast connection as well as at the connection-to-foundation interface. Under these assumptions, the model described below was implemented in the finite element program Diana 10.6 (DIANA - Finite Element Analysis, 2022)

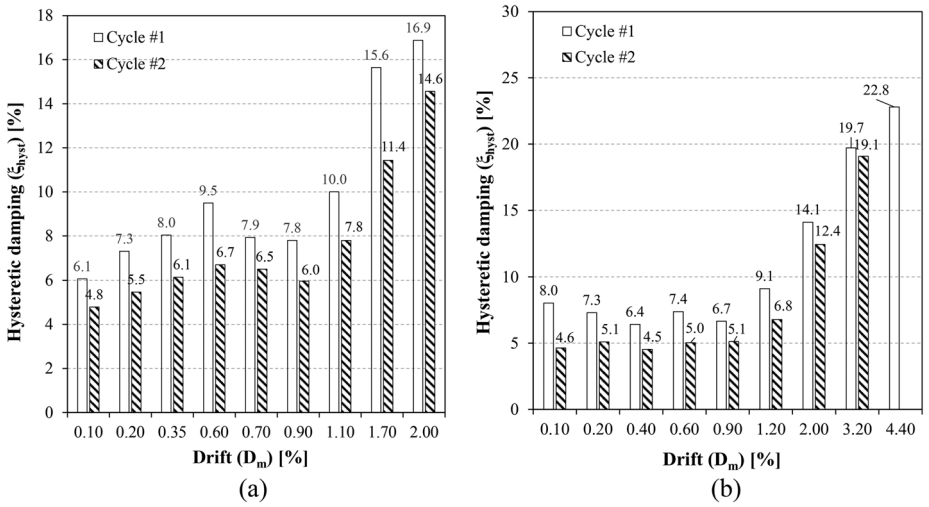

Fig. 13 Hysteretic damping factors corrected according to Priestley et al. (2007): (**a**) specimen PC1; (**b**) specimen PC2

and then used to simulate the specimens under monotonic conditions. The results will be compared to the experimental load-deflection envelope curves to assess the reliability of the model. It is worth remarking that the simplicity of the model precludes a detailed representation of the test specimens' overall response. Instead, it is expected to provide a reasonable representation of some key parameters like the initial lateral stiffness, the maximum resistance and the deflection capacity.

5.1 Description of the lumped plasticity model

To simulate the response of the test columns, the simple lumped plasticity beam model described in the previous section was implemented in the program Diana 10.6. As shown in the schematic of Fig. 11, the specimen, which includes both the column and the precast connection, is subdivided into two beam elastic elements. The nonlinear behavior is lumped in plastic hinges modelled by rotational spring elements. A rotational spring element ("BS") is located at the base of the column to capture the potential non-linear response of the interface between the column and the foundation. A stiff beam element connects the spring "BS" to the rotational spring "JS" representing the precast joint. The spring "JS" is aligned with the top end of the steel shoes laying at 295 mm from the top side of the foundation. This spring is connected to the linear elastic beam element "EB" having the same material (E_{cm}, Poissons's coefficient $\nu = 0.2$) and cross-sectional properties of the RC column. Moment (M) – Rotation (θ) laws must be implemented to represent the response of the two rotational springs. These laws were here derived from the analysis of the cross sections at hinge location performed by the sectional analysis program "Response-2000" developed by Bentz (2000).

A $600 \times 600\,mm^2$ concrete section containing the four corner threaded rods (M30) and the intermediate rebars, if any, was considered to represent the column-to-foundation interface corresponding to the hinge "BS". Figure 14a and b show the geometrical properties of the

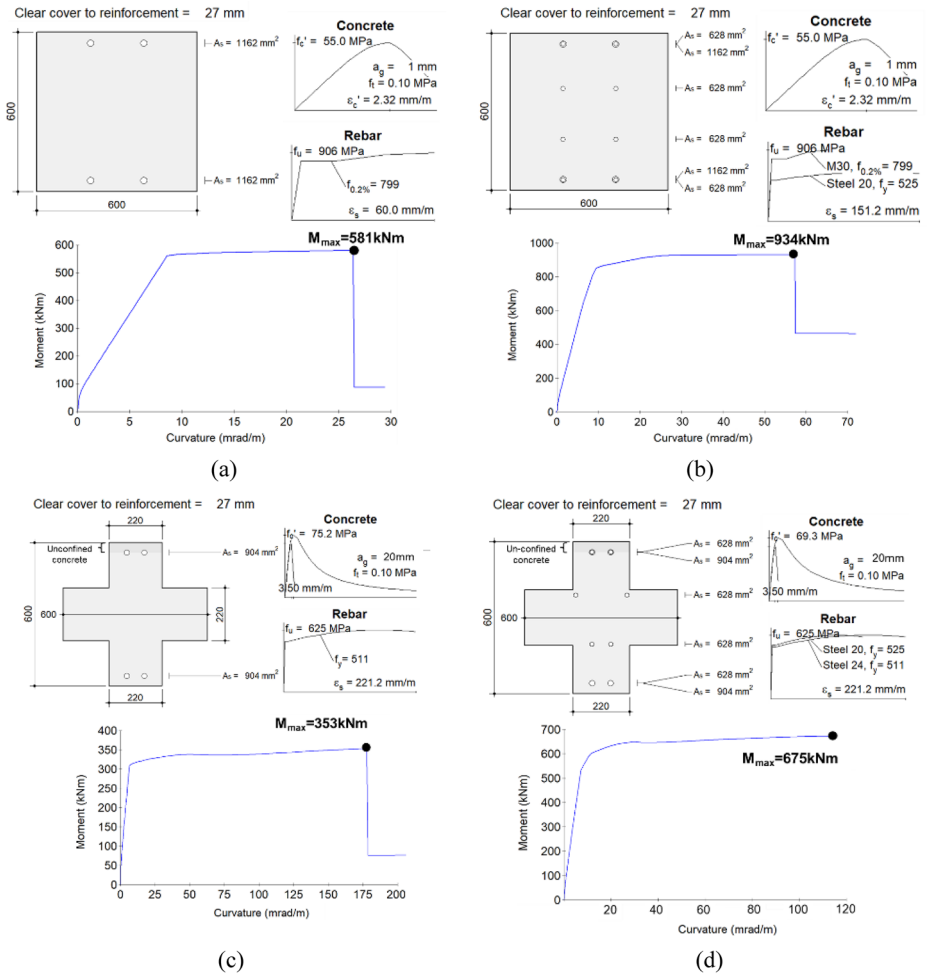

Fig. 14 Properties of cross-sections and moment-curvature curves obtained by the cross-sectional analysis with Response-2000: (**a**) specimen PC1, spring "BS"; (**b**) specimen PC2, spring "BS"; (**c**) specimen PC1, spring "JS"; (**d**) specimen PC2, spring "JS"

cross section as well as the constitutive laws of materials. About the compressive behavior, the Popovic's stress-strain curve was adopted, considering the same mean compressive strength of the cement grout (f_{cm}=55.3 MPa), both for PC1 and PC2. As no specific tests on the rods M30 (class 8.8) were performed in this research, the uniaxial tensile behavior of steel was determined according to the nominal stress-strain curve reported by Bursi & Jaspart (1997) for bolts having a yield strength of about 800 MPa, an ultimate strength of 906 MPa and a corresponding ultimate strain of 6%. Based on the mean tensile properties of rebars Ø20 (Table 1), a tri-linear stress-strain law with hardening was adopted for the intermediate rebars of PC2. An elastic modulus of 200 GPa was assumed for both bar typologies. The Moment (M) – Curvature (χ) curves resulted from the cross-section analysis are depicted in Figure 14a and b.

To turn the M(χ) curves into the corresponding M(θ) curve of the spring "BS", the displacement components (δ) reported in the schematic of Figure 15 were considered. That is, for each value of M forming the M(χ), the angle θ was obtained from the following equation:

$$\theta = \delta_{\mathrm{BS}}/\mathrm{d} \tag{6}$$

where d = 559 mm is the distance from the extreme compressed fiber to the rods/rebars located on the tension side of the base section; δ_{BS} is the total vertical displacement of the base plate derived from the following relation:

$$\delta_{\mathrm{BS}} = \delta_{\mathrm{rod}} + \delta_{\mathrm{slip}} + \delta_{\mathrm{grout}} \tag{7}$$

where $\delta_{\mathrm{rod}} = \varepsilon_{\mathrm{s}} \cdot \mathrm{L}_{\mathrm{rod}}$ is the maximum elongation of the rebars/rods; ε_{s} is the rebars strain resulting from sectional analysis; $\mathrm{L}_{\mathrm{rod}}$ is the distance between the top face of the foundation and the nut-washer assembly clamping the corner threaded bars ($\mathrm{L}_{\mathrm{rod}} = 90$ mm). For the intermediate rebars, $\mathrm{L}_{\mathrm{rod}}$ was assumed equal to the thickness ($\mathrm{L}_{\mathrm{g}} = 50$ mm) of the grout layer filling the gap between the joint and the foundation.

The slip (δ_{slip}) exhibited by the tension bars anchored to the foundation can be estimated according to the fib Bulletin n.43 (par. 7.2.3) (2004) for the end-slip response of ribbed bars. By rearranging the formulations reported in (E.C. Bentz 2000), the following relationships are obtained:

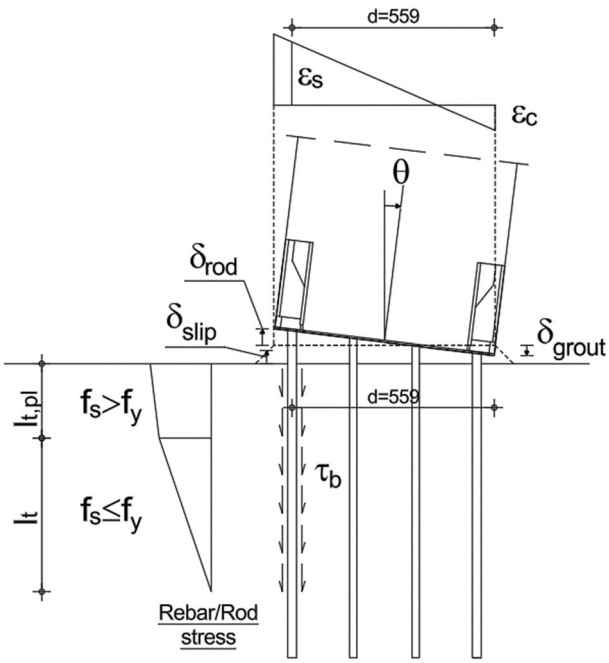

Fig. 15 Schematic of stress and strain components acting at the column-to-foundation base section. (dimensions in [mm])

$$\delta_{slip} = \begin{cases} 0.288 \cdot \left(\dfrac{\phi_b f_s^2}{\tau_{b,\max} E_s} \right)^{0.714} + \dfrac{f_s}{E_s} \cdot 2\phi_b & \text{for} \quad \delta_{slip} \le \delta_{slip,y} \quad (8) \\ 0.5\delta_{slip,u} - (0.5\delta_{slip,u} - \delta_{slip,y}) \cdot \dfrac{f_s - f_u}{f_{y0} - f_u} & \text{for} \quad \delta_{slip,y} < \delta_{slip} \leqslant 0.5\delta_{slip,u} \quad (9) \\ 0.5\delta_{slip,u} + \delta_{slip,u} \cdot \dfrac{f_u - f_s}{f_u} & \text{for} \quad 0.5\delta_{slip,u} < \delta_{slip} \le \delta_{slip,u} \quad (10) \end{cases}$$

where f_s is the actual tensile stress acting in the rebars/rods; $\tau_{b,max}$ is the maximum bond-strength here assumed equal to $2.5\sqrt{f_{cm}}$ (good-bond conditions); $Ø_b$ is the nominal diameter of rebars/rods; $E_s = 200$ GPa is the Young's modulus of steel; f_u and f_y are respectively the ultimate and the yield strength of steel, as reported in Table 1; f_{cm} is the mean cylindrical compressive strength of concrete (Table 1). The Eq. (8), which is valid as long as the slip remains lower than 1 mm, provides the end-slip of the rebar in the elastic stage. On the contrary, when the end-slip attains the value $\delta_{slip,y}$, rebars start yielding and the slip can be calculated by the Eq. (9). The end-slip $\delta_{slip,y}$ is simply obtained by replacing f_s with f_y in the Eq. (8). The Eq. (9) depends on the ultimate slip $\delta_{slip,u}$ that results from the following relation:

$$\delta_{\mathrm{slip,u}} = \left(\frac{f_u - f_y}{0.27 \cdot \tau_{\mathrm{b,max}}} \right) \cdot \frac{Ø_b}{8} \cdot \varepsilon_u + \delta_{\mathrm{slip,y}} \quad (11)$$

where ε_u is the ultimate strain of steel rebars reported in Table 1. The original formulation reported in the fib Bulletin n.43 (2004) assumes that the after attaining the end-slip $0.5\delta_{slip,u}$, the tensile stress of rebar remains equal to f_u until the slip reaches $\delta_{slip,u}$. To be more conservative, the method here proposed assumes a linear decrease in rebar stress to zero over this slip range, leading to Eq. 10 . Finally, considering the maximum compressive strain (ε_c) acting in the extreme compressed fiber of the base section, the compressive deflection of grout can be assumed equal to:

$$\delta_{\mathrm{grout}} = L_g \cdot \varepsilon_c \quad (12)$$

The stress (f_s) and the strains (ε_s; ε_c) required by the previous equations were obtained from the sectional analysis performed with Response-2000 for increasing values of the curvature. Thus, once the Eqs. (6)-(11) were implemented, the $M_{(\theta)}$ of Figure 16a were obtained. Note that after attaining the maximum moment (M_{max}), it was conservatively assumed that the rotational capacity drops to 20% of M_{max}.

To define the $M_{(\theta)}$law referred to the spring "JS", the flexural response of the concrete section located in the middle of the joint was investigated. As shown in Figure 14c and d, the section has a cross-shape geometry corresponding approximately to the concrete area located among the four steel shoes. Both for PC1 and PC2 the confinement effect provided by the stirrups was taken into account by the stress-strain model for concrete in compression recommended by Mander et al. (1988). The latter was assigned only to the concrete area enclosed within the centerline of the stirrups, while the stress-strain law for unconfined concrete was attributed to the concrete cover. The curvatures resulting from the sectional analysis were turned into the corresponding rotations by the following relations suggested by Priestley et al. (2007):

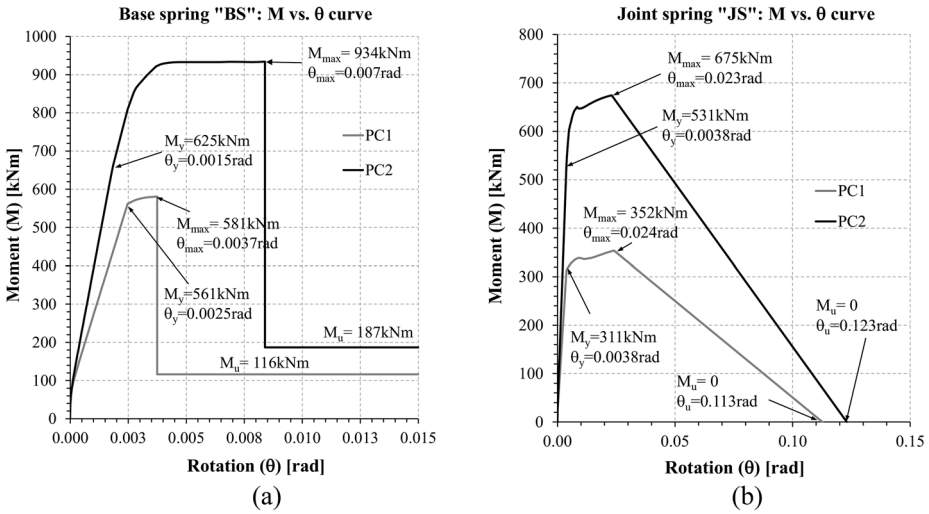

Fig. 16 Moment-rotation laws attributed to the rotational springs (**a**) "BS" and (**b**) "JS"

$$\theta_{cr}=\frac{L_{JS}}{3}\cdot\chi_{cr}\quad first-cracking \tag{13}$$

$$\theta_{y}=\frac{L_{JS}}{3}\cdot\chi_{y}\quad yielding \tag{14}$$

$$\theta=\theta_{y}\frac{M_{(\chi)}}{M_{y}}+L_{PT}\left(\chi-\chi_{y}\frac{M_{(\chi)}}{M_{y}}\right)\cdot\left(1-0.5\frac{L_{PT}}{L_{JS}}\right)\quad \theta_{y}<\theta\leq\theta_{max} \tag{15}$$

$$\theta=M_{max}\cdot\frac{\theta-\theta_{u}}{\theta_{max}-\theta_{u}}\quad \theta_{max}<\theta\leq\theta_{u} \tag{16}$$

where χ_{cr} is the curvature at first cracking; χ_y and M_y are the curvature and the corresponding moment at first yielding of longitudinal reinforcement; θ_{cr} and θ_y are the rotations at first cracking and yielding; θ_{max} is the rotation corresponding to the maximum moment M_{max}; $L_{JS}=1610$ mm (Fig. 11) is the distance from the lateral load to the hinge "JS". According to Eq. (4) L_{PT} is equal to 123 mm and 187 mm for specimen PC1 and PC2, respectively.

Equations (13)-(15) allow determining the $M_{(\theta)}$ law up to the rotation θ_{max}. For rotations higher than θ_{max} the moment linearly reduces to zero according to the Eq. (16). The ultimate rotation θ_u can be calculated by the following equation proposed by Ibarra et al. (2005):

$$\theta_{u}-\theta_{max}=0.76\cdot(0.031)^{n}\cdot(0.02+40\rho_{sh})^{1.02}\leq 0.1\text{rad} \tag{17}$$

where $\rho_{sh}=0.75\%$ is the transverse steel ratio and $n=0.016$ corresponds to the axial load ($N=300$ kN) to the axial resistance ($N_R=18750$ kN) ratio of the column section. The $M_{(\theta)}$ curves assigned to the rotational spring "JS" of PC1 and PC2 are shown in Fig. 16b.

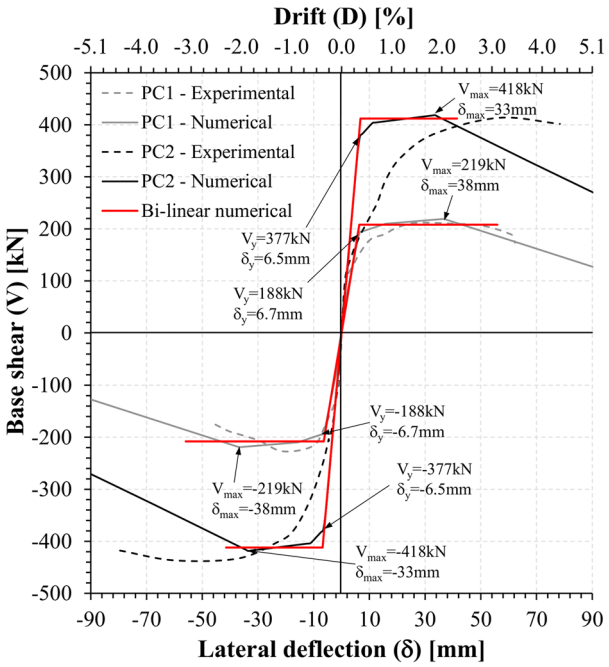

Fig. 17 Base shear vs. lateral deflection: comparison between experimental and numerical response

After implementing the beam model of Figure 11 in the program Diana 10.6, the two test specimens were simulated by monotonically increasing the lateral deflection applied to the top of the column. The results of the simulations are discussed in the following section.

5.2 Results of the simulations and discussion

Figure 17 compares the numerical load-deflection response calculated by the simplified lumped plasticity model with the experimental envelope curves. As expected, the response of the columns was mainly governed by the hinge "JS" that attained its maximum capacity before the hinge "BS". The numerical model accurately captured the initial elastic branch of the experimental curves. However, after cracking, the model tended to overestimate the lateral stiffness, although this overprediction aligns well with the stiffness K^* of the bi-linear curves. The points on the numerical curves marked with the labels V_y and V_{max} correspond respectively to the attainment of the yield Moment (M_y) and the maximum moment (M_{max}) (see also Fig. 16b) at the level of the hinge "JS".

The model's weakest prediction was for specimen PC2, which exhibited an unexpected stiffness loss within the deflection range +2 mm/+8 mm, as described in Sect. 3. Despite this, the maximum capacity and the corresponding deflection in the numerical curves closely matched those observed experimentally. As shown in Fig. 17, the peaks of the numerical curves correspond to maximum base shear values of 219 kN and 418 kN for PC1 and PC2, respectively. These values are only 5% and 2% higher than the corresponding experimental values reported in Table 2. The maximum numerical deflection attained by PC2 (i.e., $\delta_{max}=33$ mm) was more than 50% lower than the mean experimental value. For PC1, the maximum deflection (i.e., $\delta_{max}=38$ mm) was 65% higher than the corresponding mean

experimental value. Regarding the post-peak response, the progressive resistance decay observed in specimen PC1 was reasonably consistent with the model's predictions. For PC2, the model's prediction was notably conservative, with a stiffness and resistance reduction that resulted to be more pronounced than that observed experimentally.

Figure 17 also reports the red curves representing the bilinearization of the numerical responses. To maintain consistency with the experimental bilinear curves shown in Fig. 9a, the ultimate deflection used for the bilinear approximation corresponds to a post-peak strength degradation of 15% for PC1 and 5% for PC2. Based on these curves, the ductility index (μ_δ) resulted equal to 8.8 for PC1 and 6.1 for PC2. These values differ by less than 15% from the experimental displacement ductility reported in Table 2.

In conclusion, the model provided a reasonably accurate prediction of the actual response. Further investigation may be useful to improve the model's ability in predicting the post-peak response.

6 Conclusions

Two experimental tests on a foundation shoe connection for precast columns were presented and discussed in this paper. The two specimens differed in the number of column longitudinal bars bonded to the foundation. In PC1 the column was connected only through four corner bolted steel shoes whereas PC2 incorporated both the four corner shoes and additional intermediate bars along the four sides of the column cross-section. Sample PC1 did not represent a typical connection configuration used in practice but it was tested to highlight the structural performance of the steel shoes themselves. In specimen PC2, on the contrary, the novel combination of corner shoes and intermediate grouted bars represents a novel connection.

Based on the experimental results and the related discussion, the following main conclusions can be drawn:

- The adoption of the corner shoe connection investigated in this study does not result in any significant reduction in ductility, energy dissipation, or displacement capacity.
- Aside from a higher number of flexural cracks in the concrete, likely due to the greater longitudinal reinforcement ratio in specimen PC2, the damage observed at the column base was similar in both specimens.
- Bilinearization of the envelope curves for the two specimens revealed that PC2 exhibited a 59% greater deflection δ_{NC} than PC1, indicating higher displacement capacity. However, the displacement ductility index of PC2 was 45% lower than that of PC1. This decrease in ductility can be attributed to the higher tensile reinforcement ratio in PC2 ($\rho_s = 0.54\%$) compared to PC1 ($\rho_s = 0.19\%$) as well as to the early loss of initial stiffness exhibited by PC2 during positive loading.
- A simple yet effective plasticity-based analytical model, applied through a numerical program, provided a fairly accurate estimation of both load and displacement capacities. Specifically, the predicted maximum base shear and displacement ductility values differed by less than 5% and 15%, respectively, from the corresponding mean experimental results. The prediction of lateral deflection at maximum resistance was less accurate, though still reasonable. This model can be readily implemented in any finite element

program. However, further refinement is recommended, particularly to improve the accuracy of the post-peak response prediction.

Acknowledgements The Authors would like to thank Baraclit S.p.a. and its engineering team, including Luca Bernardini, Patrizio Alberti, Francesco Bussi, Paolo Panoni and Cristina Rimbotti, for the financial and technical support provided to this research. Thanks go also to Giovanni Bono who designed the connection system adopted herein. Eventually, the help of Andrea Delbarba, technician of the Laboratory "P. Pisa" of the University of Brescia, is also gratefully acknowledged.

Author contributions The authors contributed to the present work as follows: Luca Facconi: Conceived and designed the experimental study; developed the analytical model; assisted in the execution of the tests; analyzed the experimental results; prepared the first draft of the manuscript. Paolo Pizzini: Prepared materials; carried out the experimental tests; conducted post-processing of the experimental data. Fausto Minelli: Secured the funding for the research; Conceived and designed the experimental study; interpreted the experimental data; revised the manuscript. All authors have read and approved the final version of the manuscript.

Funding Open access funding provided by Università degli Studi di Brescia within the CRUI-CARE Agreement. This work was supported by the company Baraclit S.p.a., which provided both technical and financial resources to perform the experimental investigation.

Data availability The datasets obtained from the present experimental and analytical work are available from the corresponding author on reasonable request.

Declarations

Competing interests The authors have no relevant financial or non-financial interests to disclose.

References

Belleri A, Brunesi E, Nascimbene R, Pagani M, Riva P (2015) Seismic performance of precast industrial facilities following major earthquakes in the Italian territory. J Perform Constructed Facil 29(5):04014135

Belleri A, Riva P (2012) Seismic performance and retrofit of precast concrete grouted sleeve connections. Pci J 57(1)

Bursi OS, Jaspart JP (1997) Benchmarks for finite element modelling of bolted steel connections. J Constructional Steel Res 43(1–3):17–42

Chopra AK (2011) Dynamics of structures, Fourth edn. Prentice Hall

Cimmino M, Magliulo G, Manfredi G (2020) Seismic collapse assessment of new European single-story RC precast buildings with weak connections. Bull Earthquake Eng 18(15):6661–86

COMM2019 (2019) Circolare n. 7 del 21 gennaio 2019: istruzioni per l'applicazione dell'aggiornamento delle Norme tecniche per le costruzioni di cui al Decreto ministeriale 17 gennaio 2018. Ministry of Infrastructures and Transportations, Rome, Italy. (in Italian)

Dal Lago B, Negro P, Dal Lago A (2018) Seismic design and performance of dry-assembled precast structures with adaptable joints. Soil Dyn Earthquake Eng 106:182–95

Dal Lago B, Toniolo G, Lamperti Tornaghi M (2016) Influence of different mechanical column-foundation connection devices on the seismic behaviour of precast structures. Bull Earthquake Eng 14(12):3485–508

Deng X, Wang S, Chen J, Ding FX, Zhang Q, Xiang P (2022) Experimental investigation on the effect of local debonding of longitudinal reinforcement on seismic performance of precast concrete columns. J Building Eng 46:103131
DIANA – Finite Element Analysis (2022). User's Manual - Release 10.6. DIANA FEA BV, Thijsseweg 11, 2629 JA Delft, The Netherland
E.C. Bentz (2000). Sectional analysis of reinforced concrete members 184. PhD thesis, Department of Civil Engineering, University of Toronto, Toronto, ON, Canada https://www.hadrianworks.com/
EN 10025-2:2019. Hot rolled products of structural steels - Part 2: Technical delivery conditions for non-alloy structural steels.
EN 196-1:2016. Methods of testing cement - part 1: Determination of strength
EN 1990: 2023 Eurocode: Basis of structural design
EN 1992-1-1:2023, Eurocode 2. Design of concrete structures. Part 1–1: general rules and rules for buildings, bridges and civil engineering structures
EN 1998-1:2004, Eurocode 8: design of structures for earthquake resistance - part 1: General rules, seismic actions and rules for building
EN ISO :2013. Mechanical properties of fasteners made of carbon steel and alloy steel part, 1: bolts, screws and studs with specified property classes - coarse thread and fine pitch thread.
EN ISO 2553:2019. Welding and allied processes - Symbolic representation on drawings - Welded joints
Fan JJ, Feng DC, Wu G, Hou S, Lu Y (2020) Experimental study of prefabricated RC column-foundation assemblies with two different connection methods and using large-diameter reinforcing bars. Eng Struct 205:110075
FEMA 461 (2007). Interim testing protocols for determining the seismic performance characteristics of structural and nonstructural components . Federal Emergency Management Agency, Washington, DC, USA
fib Bulletin No. 43 (2004). Structural connections for precast concrete buildings. Guide to good practice (ISBN 978-2-88394-083-3)
Ibarra LF, Medina RA, Krawinkler H (2005) Hysteretic models that incorporate strength and stiffness deterioration. Earthquake Eng Struct Dyn 34:1489–511
Jacobsen L S (1960) Damping in composite structures. In Proceeding, 2nd World Conference on Earthquake Engineering, 2, Tokyo and Kyoto, Japan, 1029–44, 1960
Kurama YC, Sritharan S, Fleischman RB, Restrepo JI, Henry RS, Cleland NM, et al. (2018) Seismic-resistant precast concrete structures: state of the art. J Struct Eng 144(4):03118001
Liu Z, Lei H, Tong T, Wu S, Lu G (2022) Precast segmental piers: testing, modeling and seismic assessment of an emulative connection based on a grouted central tenon. Bull Earthquake Eng 20(5):2529–64
Magliulo G, Ercolino M, Petrone C, Coppola O, Manfredi G (2014) The Emilia earthquake: seismic performance of precast reinforced concrete buildings. Earthquake Spectra 30(2):891–912
Mander JB, Priestley MJ, Park R (1988) Theoretical stress-strain model for confined concrete. J Struct Eng 114(8):1804–26
Metelli G, Beschi C, Riva P (2011) Cyclic behaviour of a column to foundation joint for concrete precast structures. Eur J Environ Civ Eng 15(9):1297–318
Nascimbene R, Bianco L (2021) Cyclic response of column to foundation connections of reinforced concrete precast structures: numerical and experimental comparisons. Eng Struct 247:113214
NTC2018 -Norme Tecniche per le Costruzioni (2018). Decreto ministeriale del 17/01/18-Aggiornamento delle Norme Tecniche per le Costruzioni, 17 gennaio 2018. (In Italian
Park R, Paulay T (1975) Reinforced concrete structures. J. Wiley Sons. ISBN: 0-471-65917-7
Paulay T, Priestley MJN (1992) Seismic design of reinforced concrete and masonry buildings. John Wiley & Sons, Inc. ISBN: 9780471549154, Online ISBN: 9780470172841
Priestley MJN, Calvi GM, Kowalsky MJ (2007) Displacement based seismic design of structures. IUSS Press, Pavia, Italy, 2007. ISBN 10: 8861980007; ISBN 13: 9788861980006
Pul S, Senturk M, Ilki A, Hajirasouliha I (2021) Experimental and numerical investigation of a proposed monolithic-like precast concrete column-foundation connection. Eng Struct 246:113090
Savoia M, Buratti N, Vincenzi L (2017) Damage and collapses in industrial precast buildings after the 2012 Emilia earthquake. Eng Struct 137:162–80
Toniolo G, Colombo A (2012) Precast concrete structures: the lessons learned from the L'Aquila earthquake. Struct Concr 13(2):73–83
Tullini N, Minghini F (2020) Cyclic test on a precast reinforced concrete column-to-foundation grouted duct connection. Bull Earthquake Eng 18(4):1657–91
UNI EN ISO 15630-1:2019 Acciaio per calcestruzzo armato e calcestruzzo armato precompresso - Metodi di prova - Parte, 1: Barre, rotoli e fili per calcestruzzo armato. (n Italian)

Authors and Affiliations

Luca Facconi[1] · Paolo Pizzini[1] · Fausto Minelli[1]

✉ Luca Facconi
luca.facconi@unibs.it

Paolo Pizzini
paolo.pizzini@unibs.it

Fausto Minelli
fausto.minelli@unibs.it

[1] Department of Civil, Environmental, Architectural Engineering and Mathematics (DICATAM), Università di Brescia, Brescia, Italy